frontiers | Frontiers in Mechanical Engineering

TYPE Original Research
PUBLISHED 02 January 2026
DOI 10.3389/fmech.2025.1735111

OPEN ACCESS

EDITED BY
Utkarsh Chadha,
University of Toronto, Canada

REVIEWED BY
F. Khan,
King Faisal University, Saudi Arabia
Akshansh Mishra,
Polytechnic University of Milan, Italy
Mohammad Azami,
Concordia University, Canada

*CORRESPONDENCE
Jaka Burja,
jaka.burja@imt.si

RECEIVED 29 October 2025
REVISED 07 December 2025
ACCEPTED 15 December 2025
PUBLISHED 02 January 2026

CITATION
Bajželj A and Burja J (2026) Microstructure of horizontally continuously cast Stellite rods. *Front. Mech. Eng.* 11:1735111. doi: 10.3389/fmech.2025.1735111

Microstructure of horizontally continuously cast Stellite rods

Anže Bajželj[1,2,3] and Jaka Burja[1,2]*

[1]Institute of Metals and Technology, Ljubljana, Slovenia, [2]Faculty of Natural Sciences and Engineering, University of Ljubljana, Ljubljana, Slovenia, [3]Metal Tech Solutions, Celje, Slovenia

This study investigates the microstructural and phase characteristics of Stellite 6, Stellite 12, and Stellite 21 alloys produced by horizontal continuous casting. The alloys were synthesized from pure metallic elements and ferroalloy (FeW) under an argon atmosphere and solidified in a water-cooled copper mould (Ø3.3 mm–Stellite 6 and Stellite 21, and Ø6.1 mm–Stellite 12), resulting in extremely high cooling rates and fine-grained microstructures. Thermodynamic calculations were performed to predict equilibrium solidification, which was compared with experimental microstructural observations. Optical and scanning electron microscopy (SEM-EDS) analyses revealed Co-rich dendritic grains surrounded by eutectic regions containing carbides of the M_7C_3, $M_{23}C_6$, and M_6C types. X-ray diffraction (XRD) confirmed the presence of an FCC Co matrix without HCP phase formation, attributed to rapid solidification. The volume fraction of carbides increased with carbon content, influencing hardness. Vickers hardness measurements showed that Stellite 6 exhibited the highest hardness (508 HV10), followed by Stellite 12 (470 HV10) and Stellite 21 (345 HV10). The finer grain size and higher carbide fraction in alloys with greater carbon content contributed to enhanced hardness and structural uniformity. These findings demonstrate that horizontal continuous casting enables the production of fine-grained Stellite rods with a homogeneous composition. The cast rods show excellent structural integrity and are well-suited for subsequent hard-facing applications in wear-resistant environments.

KEYWORDS

carbides, hard facing, horizontal continuous casting, microhardness, Stellite

1 Introduction

Stellite alloys belong to the group of cobalt-based superalloys, known for their excellent oxidation and wear resistance (Davis, 2000). These properties, combined with good biocompatibility, make Stellite suitable for medical applications, such as implants (e.g., hip, knee, and dental replacements) (Saldívar-García and López, 2005; Kurosu et al., 2010; Hu et al., 2014; Narushima and Ueda, 2015; Lu et al., 2016; Nová et al., 2017; Tunthawiroon and Chiba, 2019; Li et al., 2025). Stellite is commonly welded onto mechanical components to enhance their performance and extend their service life. These alloys are widely used in the energy, oil, wood, automotive, and aerospace industries. Thin deposited layers on component surfaces provide outstanding wear, oxidation, and corrosion resistance, even at elevated temperatures (Frenk and Kurz, 1994; Davis, 2000; Aoh and Chen, 2001; Radu et al., 2004; Radu and Li, 2005; Kapoor et al., 2012; Liu et al., 2015; Roy et al., 2021; Smolina and Kobiela, 2021).

In addition to cobalt, Stellites contain a substantial amount of chromium (typically 25–33 wt%), which imparts exceptional oxidation resistance both at room and elevated temperatures. The chromium content is sufficiently high to form a compact Cr_2O_3 oxide

film on the surface, which prevents further oxidation and degradation of the material (Phalnikar et al., 1956; Kofstad and Hed, 1969a; Kofstad and Hed, 1969b; Codaro et al., 2000; Davis, 2000; Kapoor et al., 2012; Li et al., 2013; Hu et al., 2014; Tunthawiroon et al., 2020). Apart from this protective effect, chromium also contributes to the solid solution strengthening of the matrix (Shin et al., 2003; Pala et al., 2017). Other key elements that enhance solid solution strengthening include tungsten (W) and molybdenum (Mo), which are typically added separately to the alloy. Stellites are generally categorised into Co-Cr-W alloys, which offer superior wear resistance, and Co-Cr-Mo alloys, which provide better corrosion resistance (Kuzucu et al., 1997; Davis, 2000; Shin et al., 2003; Huang et al., 2007; Kapoor et al., 2012; Hu et al., 2014; Motallebzadeh et al., 2015; Narushima and Ueda, 2015; Liu et al., 2015).

Despite solid solution strengthening, the matrix of Stellite alloys remains relatively soft and not inherently wear-resistant. Their wear resistance is primarily provided by the presence of carbides, which are crucial in these alloys (Shin et al., 2003; Huang et al., 2007; Kapoor et al., 2012; Nová et al., 2017; Ravi Kumar et al., 2020; Ahmed, De Villiers Lovelock and Davies, 2021; Chen et al., 2024; Khan et al., 2025). The carbon content typically ranges from 0.2 to 3.5 wt%, directly influencing the alloy's wear resistance (Krell et al., 2020). Stellites with lower carbon content are used in more corrosive environments–for instance, Stellite 21, which, in addition to good corrosion resistance, also offers excellent creep resistance (Davis, 2000; Huang et al., 2007; Liu et al., 2015; Zhao et al., 2024). Alloys with higher carbon content, such as Stellite 12 and Stellite 6, contain a larger volume fraction of carbides and are thus preferred for wear-resistant applications (Kuzucu et al., 1997; Shin et al., 2003; Hou et al., 2005; Kapoor et al., 2012; Motallebzadeh et al., 2015; Liu et al., 2015; Smolina and Kobiela, 2021; Karthik et al., 2022; Chen et al., 2024).

Carbides in Stellites form during the final stages of solidification, resulting in a eutectic structure with the Co-FCC phase. The proportion of eutectic and therefore carbides is relatively high, and the carbide network within the interdendritic regions contributes significantly to the wear resistance of these alloys. The most common carbides are chromium-rich M_7C_3 and $M_{23}C_6$ types (where M = Cr, Co). M_7C_3 carbides form during eutectic solidification and are likely present at room temperature in Stellite 6 and Stellite 12. These M_7C_3 carbides are metastable and may transform into $M_{23}C_6$ carbides during cooling (Kuzucu et al., 1997; Davis, 2000; Kapoor et al., 2012; Wang et al., 2021; Xiong et al., 2023; Yao et al., 2023; Ahmed et al., 2024; Chen et al., 2024). The addition of Mo to Stellite 6 and 12 suppresses the formation of M_7C_3 carbides, thereby favouring the formation of $M_{23}C_6$ eutectic carbides. (Kuzucu et al., 1997; Shin et al., 2003). The addition of W and Mo promotes the formation of M_6C-type carbides (where M = W, Mo, Co), which are harder and enhance the wear resistance of the alloy (Shin et al., 2003; Chen et al., 2020; Karthik et al., 2022).

In certain alloys, such as Stellite 21, intermetallic phases, most commonly Laves phases, also form and contribute to improved wear resistance and creep performance at elevated temperatures. Examples of intermetallic phases identified in Stellite 21 include Co_3Mo, $Co_3Mo_2(Cr,Si)$, and Co_2MoCr (Radu et al., 2004; Huang et al., 2007; R. Liu et al., 2015; Liu et al., 2015; Li et al., 2025).

At high temperatures, cobalt atoms adopt a face-centred cubic (FCC) crystal structure, which transforms to a hexagonal close-packed (HCP) structure below 427 °C under equilibrium conditions(Davis, 2000). The addition of alloying elements alters the transformation temperature between the FCC and HCP phases, while significantly reducing the transformation kinetics (Kuzucu et al., 1997; Davis, 2000; Kapoor et al., 2012; Narushima and Ueda, 2015; Chen et al., 2024; Li et al., 2025). Due to the sluggish transformation kinetics, both metastable FCC and HCP phases coexist in the cast microstructure at room temperature. Since the HCP phase has fewer slip systems, it is less deformable; therefore, Stellites with a higher fraction of HCP phase exhibit higher hardness and improved wear resistance. The FCC → HCP transformation in Stellites is martensitic and can occur during rapid cooling from the temperature range where the FCC phase is stable (athermal martensitic transformation). It can also occur upon annealing at elevated temperatures within the HCP stability region. Owing to the low stacking fault energy, strain-induced transformation to the HCP phase is also possible (Frenk and Kurz, 1994; Radu et al., 2004; Radu and Li, 2005; Saldívar-García and López, 2005; Huang et al., 2007; Narushima and Ueda, 2015; Chen et al., 2024). The mechanical properties of the matrix are strongly influenced by the ratio between the FCC and HCP phases, a factor particularly significant in Stellites with low carbide or intermetallic content, such as Stellite 21.

In this research, a characterisation of key representatives of the Stellite alloys was carried out. The alloys were produced using a horizontal continuous casting process, during which solidification of the melt occurs rapidly due to intensive heat transfer. The cast microstructure of Stellite rods exhibits grain sizes comparable to those found in hard-faced layers, as typically used for Stellites. This study focused on the characterisation of the fine-grained cast microstructure of cast rods. A detailed characterisation was performed on Stellite 6, 12, and 21 alloys.

2 Materials and methods

The alloys with compositions specified in Table 1 were produced using an induction furnace. Metallurgically pure elements and ferro-alloy (Co, Cr, C, Si, Mn, Mo, Ni, W, and FeW) were used to prepare each alloy. The melting of the materials was carried out under a protective Ar atmosphere. Once fully molten, the alloy was cast into rods using a horizontal continuous casting process. Stellite 6 and Stellite 21 were cast into rods with a diameter Ø3.3 mm, while Stellite 12 was cast into rods with a diameter of Ø6.1 mm. Figure 1 shows an induction furnace with a horizontal continuous caster for metallic materials. A water-cooled copper mould (crystalliser)

Abbreviations: FCC, face-centred cubic; HCP, hexagonal close-packed; HCC, horizontal continuous casting; XRD, X-ray diffraction; SEM, scanning electron microscopy; EDS, energy-dispersive X-ray spectroscopy; HV, Vickers hardness; HV10, Vickers hardness at 10 kgf; HV0.02, Vickers microhardness at 0.02 kgf; RT, room temperature.

TABLE 1 Chemical composition of cast Stellite alloys, values in wt%.

Alloy	Name	C	Si	Mn	Cr	Ni	Mo	W	Fe	Co
Stellite 6	S6	1.06	0.90	0.10	30.7	2.3	0.27	5.6	1.6	Bal.
Stellite 12	S12	1.33	0.90	0.15	29.5	2.7	0.12	8.8	2.6	Bal.
Stellite 21	S21	0.26	0.81	0.75	27.7	2.7	5.00	-	-	Bal.

FIGURE 1
Induction furnace with horizontal continuous caster.

is positioned inside the induction furnace. Before melting, the opening of the copper mould is sealed with a cold starter bar. When the melt is ready for casting, an electric motor periodically pulls the starter bar (approx. 3.5 Hz frequency) in 15 mm increments, which makes the effective cooling speed 52.5 mm/s. The molten metal fills the copper mould, where it rapidly cools and solidifies. This rapid cooling ensures directional solidification. Each newly solidified segment is welded to the preceding section of the rod. The chemical composition of the samples was determined from a section of the rod taken approximately midway through the casting process. The carbon content was determined using an ELTRA SC-800 combustion mass spectrometer (ELTRA), and the content of other elements was determined by XRF Thermo Scientific Niton XL3t GOLDD+ (Thermo Fisher Scientific, Waltham, MA, United States).

Thermodynamic calculations of the equilibrium phase composition were performed using the JMatPro9.0 software package (Sente Software Ltd., Guildford, United Kingdom). The chemical compositions used for the thermodynamic calculations are listed in Table 1. The program was employed to calculate the formation of phases during equilibrium solidification and cooling

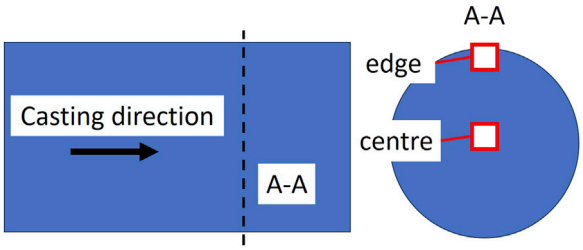

FIGURE 2
Schematic representation of the sampling procedure from the cast rods.

within the temperature range from 1500 °C to room temperature (RT).

In horizontal continuous casting, the solidification rate is relatively high, with cooling rates ranging between 200 and 2000 K/s. As a result, the crystal grains are extremely fine, and the phases form far from equilibrium conditions.

Samples for microstructural characterisation were sectioned transversely from the cast rods with respect to the casting direction. The specimens, taken from the edge and the centre as shown in Figure 2, were mounted in a bakelite resin and subsequently ground and polished. Samples were sequentially ground under water lubrication using SiC papers from 120 to 4000 grit to remove sectioning damage and achieve a uniform surface. This was followed by polishing with 6 μm, 3 μm, and 1 μm diamond suspensions on cloths, and a final chemical–mechanical polish using 0.05 μm colloidal silica to obtain a deformation-free finish. After polishing, specimens were rinsed, ultrasonically cleaned, and dried. The microstructure of the Stellite alloys was examined on ion-etched samples (10 keV, 380μA, 5 min). The metallographic analysis was performed using an Axio Imager Z2 m optical microscope (Carl Zeiss AG, Oberkochen, Germany). Additional microstructural characterization was carried out using a Thermo Fisher Scientific Apreo 2S scanning electron microscope (SEM) equipped with EDS detectors (Thermo Fisher Scientific, Waltham, MA, United States). The working parameters were 15 kV accelerating voltage, 8–15 mm working distance.

The crystalline phases present in the cast microstructures were analysed by X-ray diffraction (XRD) using a Panalytical XPert Pro PW3040/60 diffractometer (Malvern, United Kingdom). The diffraction patterns were collected from ground and polished bulk specimens over a 2Θ range of 30°–90°, with a step size of 0.002° and a time per step of 60 s. The XRD spectra were recorded using a Cu anode operated at 45 kV and 40 mA, providing $K_{\alpha1}$ radiation (λ = 1.5406 Å) and $K_{\alpha2}$ radiation (λ = 1.54443 Å) with a $K_{\alpha1}/K_{\alpha2}$ intensity ratio of 0.5.

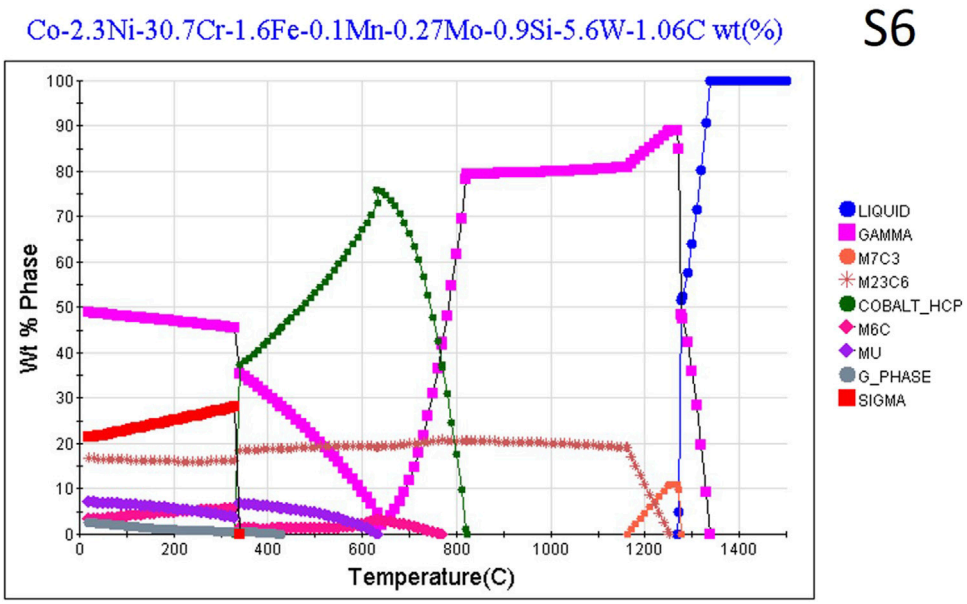

FIGURE 3
Equilibrium phase composition of S6.

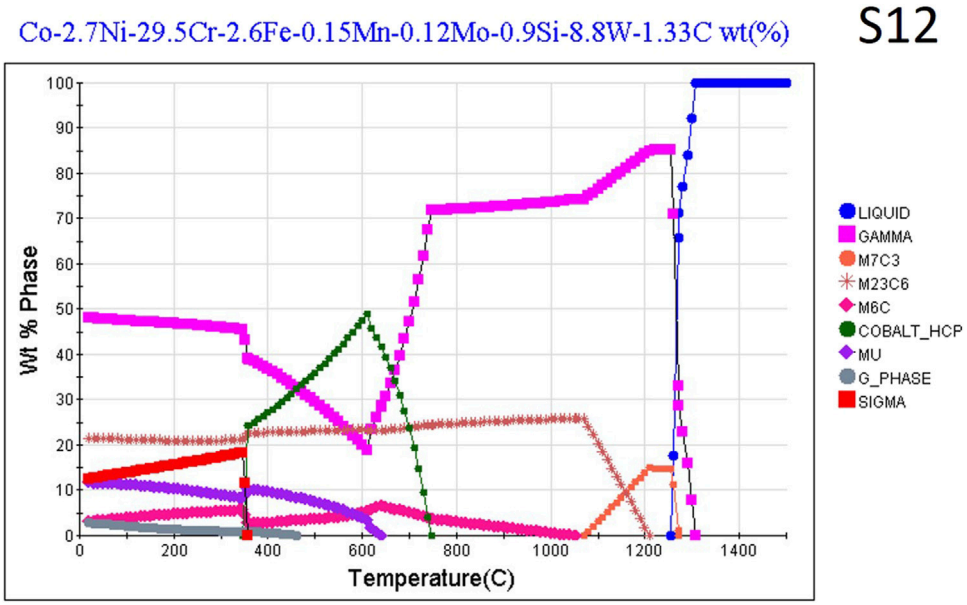

FIGURE 4
Equilibrium phase composition of S12.

Vickers hardness and microhardness of individual samples were measured using a FALCON 800G2/AO3 (INNOVATEST, Maastricht, Netherlands), in accordance with HV10 and HV0.02 standards. All three sample had at least five indentations made for HV10 and at least fifteen measurements for HV0.02. The measurements were performed in an accredited laboratory for Vickers testing SIST EN ISO 6507-1.

3 Results and discussion

3.1 Thermodynamic calculations

Figures 3–5 present the equilibrium phase diagrams for the investigated Stellite alloys. Equilibrium solidification of the S6 sample begins at a temperature of 1338 °C with the formation

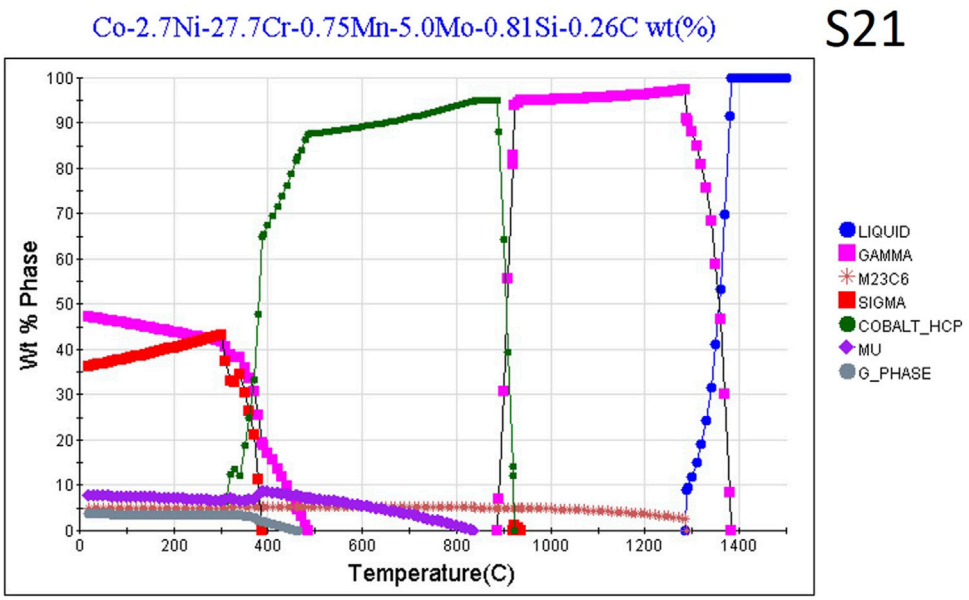

FIGURE 5
Equilibrium phase composition of S21.

of primary FCC grains of the FCC phase (GAMMA). This is followed by the eutectic solidification of a cobalt-rich phase and carbides (GAMMA + M_7C_3) at 1278 °C. The solidification concludes at 1269 °C. During cooling, a transformation of M_7C_3 carbides into $M_{23}C_6$ occurs. At room temperature, the carbide content amounts to approximately 15 wt%. At 820 °C, atomic redistribution within the matrix leads to the formation of the HCP phase, named (COBALT_HCP). Under equilibrium conditions, this phase is stable within a narrow temperature range, after which the atoms preferentially rearrange into the fcc crystal structure. Further cooling results in matrix saturation, which promotes the formation of M_6C-type carbides, rich in tungsten. Under equilibrium cooling, the intermetallic phases μ (MU) ($Co_xW_y(NiCr)_z$) and G_phase ($Ni_xSi_y(CrMn)_z$) are formed. At lower temperatures, matrix HCP (COBALT_HCP) decomposition occurs, leading to the formation of Co-rich FCC and Cr-rich (SIGMA) phases (Karaali et al., 2005).

The microstructural phases observed in the S12 alloy are similar to those identified in S6. Equilibrium solidification begins at a slightly lower temperature of 1308 °C, which can be attributed to the higher concentrations of alloying elements such as carbon and tungsten. Eutectic solidification starts at approximately 1270 °C, leading to the formation of a eutectic structure consisting of γ (GAMMA) + M_7C_3 carbides, which continues until about 1254 °C. Solidification is completed at this temperature. Upon cooling, M_7C_3 carbides transform into $M_{23}C_6$; at room temperature, their proportion slightly exceeds 20 wt%. At 1050 °C, M_6C carbides rich in tungsten begin to precipitate. At 750 °C, the HCP phase (COBALT_HCP) forms. However, due to the high content of Fe, Ni, and C, the stability of the HCP phase is limited. At lower temperatures, the matrix decomposes, and atoms are again arranged in the FCC crystal structure. In this alloy, intermetallic phases and matrix decomposition at lower temperatures also occur.

The S21 alloy contains a low carbon content, which contributes to a higher initial solidification temperature. Formation of the FCC phase begins at 1383 °C, predominantly resulting in FCC grains. At the end of solidification, at 1287 °C, a small amount of eutectic (GAMMA + $M_{23}C_6$) is formed. The content of $M_{23}C_6$ carbides at room temperature is approximately 5 wt%. The HCP (COBALT_HCP) phase is stable over a broader temperature range, with equilibrium transformation occurring at around 920 °C. Below 400 °C, the FCC and σ phases form as a consequence of matrix decomposition. Upon cooling below 830 °C, the intermetallic μ phase ($Co_xMo_y(CrSi)_z$) begins to form; at room temperature, its proportion exceeds that of the $M_{23}C_6$ carbides.

3.2 Metallography

Figures 6–8 show the microstructures of the cast Stellite samples produced by horizontal continuous casting. The figures present cross-sections taken perpendicular to the casting direction. Microstructural observations were performed both at the centre and at the outer edge of the rods. All samples exhibit shrinkage porosity in the centre of the cast rods, which results from the rapid cooling and solidification during horizontal continuous casting. Due to the high solidification rates in the water-cooled copper mould, solidification occurs separately in each stroke. The crystal grains are fine and the phases are uniformly distributed throughout the material, which is also a consequence of the extremely high cooling rates. The grains near

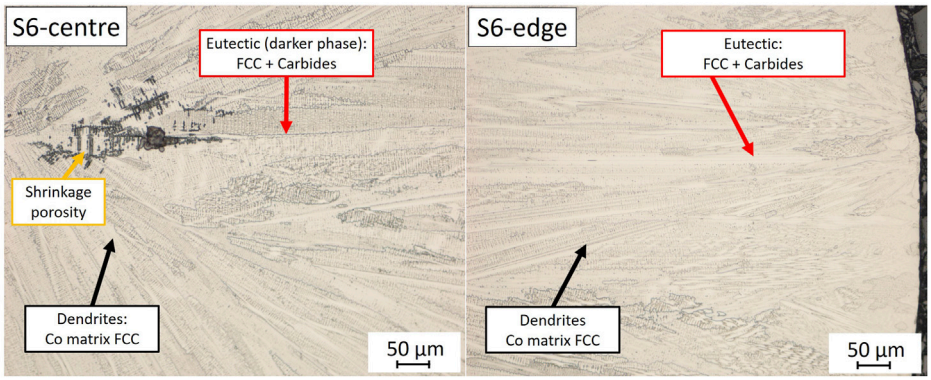

FIGURE 6
Optical microscopy of cast sample S6.

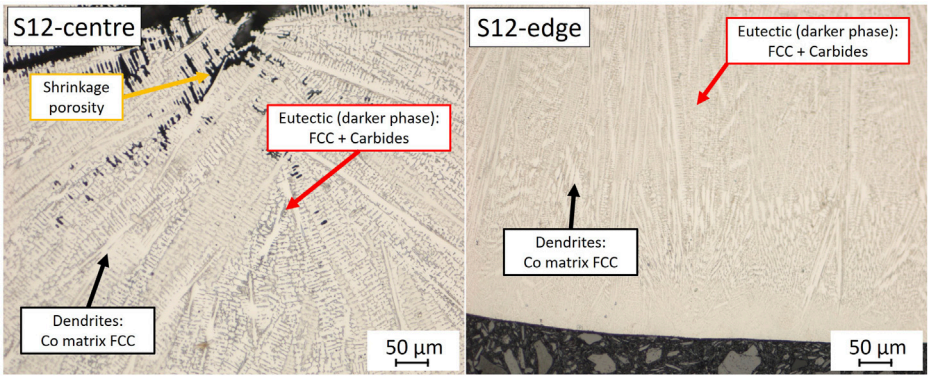

FIGURE 7
Optical microscopy of cast sample S12.

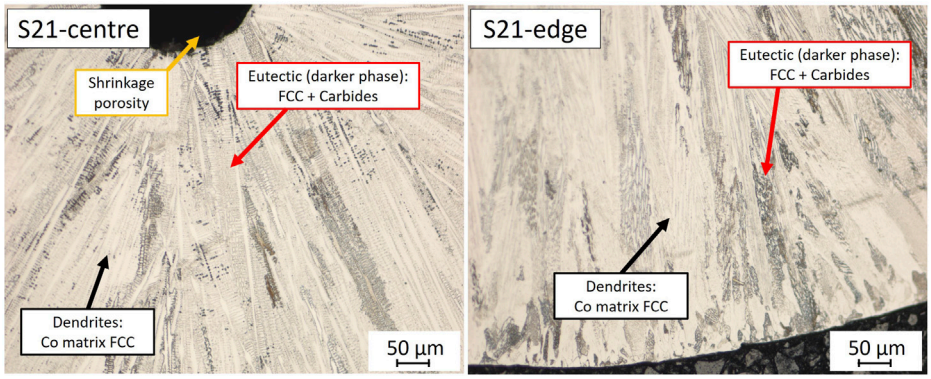

FIGURE 8
Optical microscopy of cast sample S21.

the edges are finer compared to those in the central region of the rods. Sample S12 exhibits slightly larger grains due to the larger diameter of the cast rods (Ø6.1 mm) compared to samples S6 and S21 (Ø3.3 mm). In all samples, solidification began with the formation of Co-rich dendrites (Co matrix FCC), followed by the solidification of a eutectic in the interdendritic regions. The

TABLE 2 SDAS of the S6, S12 and S21 samples.

Sample	SDAS (μm)	Calculated cooling speed (K/s)
S6 – edge	2.6 ± 0.3	$1.9{\cdot}10^{3}$
S6 – centre	3.0 ± 0.1	$1.2{\cdot}10^{3}$
S12 – edge	2.9 ± 0.6	$1.4{\cdot}10^{3}$
S12 – centre	5.7 ± 0.3	$2.0{\cdot}10^{2}$
S21 – edge	2.7 ± 0.4	$1.7{\cdot}10^{3}$
S21 – centre	3.4 ± 0.2	$8.0{\cdot}10^{2}$

eutectic consists of a Co-rich phase and carbides (FCC + Carbides), and its volume fraction increases with the carbon content in the alloy.

Studies on Cu and Fe alloys show that HCC, with its rapid cooling in water-cooled moulds, produces a transition from coarse columnar grains to finer equiaxed grains. This refinement is attributed to the higher cooling rates and solidification speeds (Bockus, 2006; Strzępek et al., 2025). HCC is promising for cobalt-based alloys, especially for high-performance applications such as medical implants and wear-resistant components. Recent research highlights the process's ability to produce high-quality Co-based alloy rods with desirable microstructural and mechanical properties.(Ahmed et al., 2024).

Secondary dendrite arm spacing (SDAS) measurements were extracted from micrographs, giving values of 2.6–3.0 μm for S6, 2.9–5.7 μm for S12, and 2.7–3.4 μm for S21 (as shown in Table 2). Using empirical correlations of Equation 1.

$$SDAS = B \cdot T^{(-n)} \quad (1)$$

where B is $29.2{\cdot}10^{-6}$ with n = 0.32 for Co-based alloys (Frenk and Kurz, 1994). The corresponding cooling rates were estimated as 1200–1900 K/s (S6), 200–1400 K/s (S12), and 800–1700 K/s (S21). These values agree well with cooling rates reported for HCC rods of similar diameters. This supports our interpretation that suppressed FCC to HCP transformation and limited M_7C_3 to $M_{23}C_6$ conversion result from rapid solidification.

3.3 Hardness and microhardness

Table 3 presents the measured hardness values of the S6, S12, and S21 in the as-cast state. The samples exhibit high hardness due to their finer grain size. The S21 sample shows the lowest hardness as a result of its low carbon content and, consequently, a lower carbide fraction. The S6 alloy was cast into rods with a diameter of Ø3.3 mm, while the S12 alloy was cast into rods with a diameter of Ø6.1 mm. The solidification of the S6 alloy sample was significantly faster, resulting in smaller crystal grains and, consequently, higher hardness compared with the S12 sample. The hardness trend (S6 > S12 > S21) correlates strongly with differences in carbide fraction, grain size, and solid-solution strengthening. Under equilibrium expectations based solely on nominal compositions, S12—with the highest carbon and tungsten content—would be expected to exhibit the highest hardness. However, the higher cooling rate in the smaller-diameter S6 rods (Ø3.3 mm) produced significantly finer dendritic grains than in S12 (Ø6.1 mm), resulting in stronger Hall–Petch grain boundary strengthening. Moreover, SEM/EDS analysis shows that S6 develops a highly refined eutectic

TABLE 3 Hardness of the S6, S12 and S21 samples.

Sample	HCC (HV10)
S6	508 ± 5.0
S12	470 ± 4.1
S21	345 ± 8.4

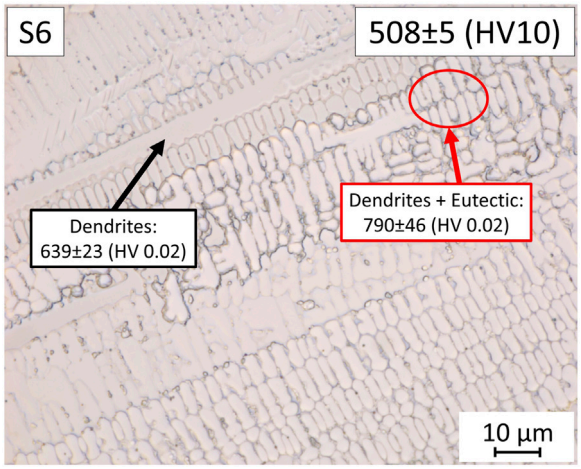

FIGURE 9
Microhardness measurements of as-cast sample S6.

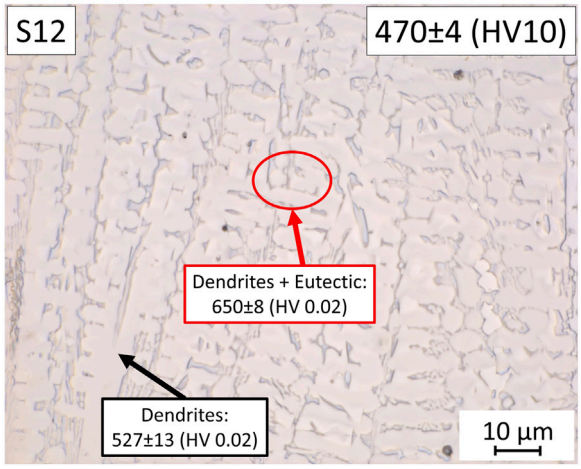

FIGURE 10
Microhardness measurements of as-cast sample S12.

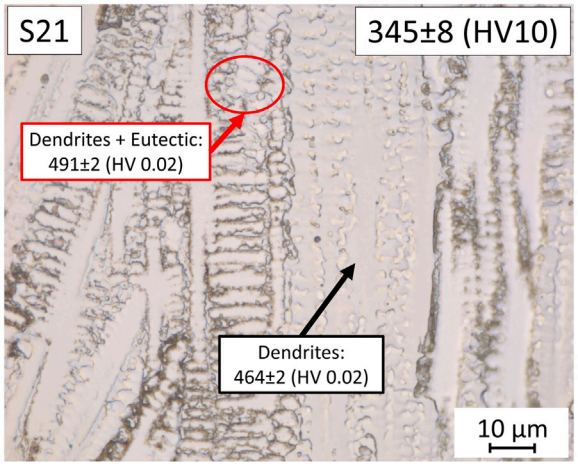

FIGURE 11
Microhardness measurements of as-cast sample S21.

network with uniformly dispersed $M_7C_3/M_{23}C_6$ carbides, while S12 exhibits coarser eutectic regions due to slightly slower solidification. The carbide morphology in S6 (fine, continuous interdendritic network) contributes more effectively to strengthening than the larger, more heterogeneously distributed carbides in S12. In contrast, S21 contains only about 5 wt% carbide and displays a predominantly solid-solution–strengthened FCC Co matrix, resulting in the lowest hardness. Additionally, differences in porosity between alloys and diameters may contribute locally to hardness scatter. Taken together, the hardness hierarchy arises not only from carbon content but from the combined effects of cooling rate, eutectic refinement, carbide morphology, and grain size.

Figures 9–11 show the microstructural images of the samples. The hardness values (HV10) are written on the upper edge of the figures, while the microhardness values (HV0.02) are shown below the individual phases. The measured HV0.02 values were slightly higher than those obtained under the higher load (HV10), which is consistent with previously reported data, where the apparent microhardness increases with decreasing applied load (Petrík and Palfy, 2011). With increasing amounts of dissolved carbon and other alloying elements, the hardness of the matrix phase increases. However, the determination of hardness for individual phases was limited, due to the fine grain size.

3.4 XRD analysis

Figure 12 shows the XRD patterns of the analysed samples. All samples exhibit an FCC Co matrix with carbides of the M_7C_3 and $M_{23}C_6$ types. No HCP Co phase was detected, indicating that the transformation to the ε phase did not occur due to the homogeneous chemical composition and the rapid cooling during solidification. In samples S6 and S12, M_7C_3 carbides predominate, formed during eutectic solidification. The rapid cooling prevented their transformation into $M_{23}C_6$ carbides. Sample S21 contains only $M_{23}C_6$ carbides, with no other intermetallic phases detected. The short cooling times hindered phase transformations in the solid state.

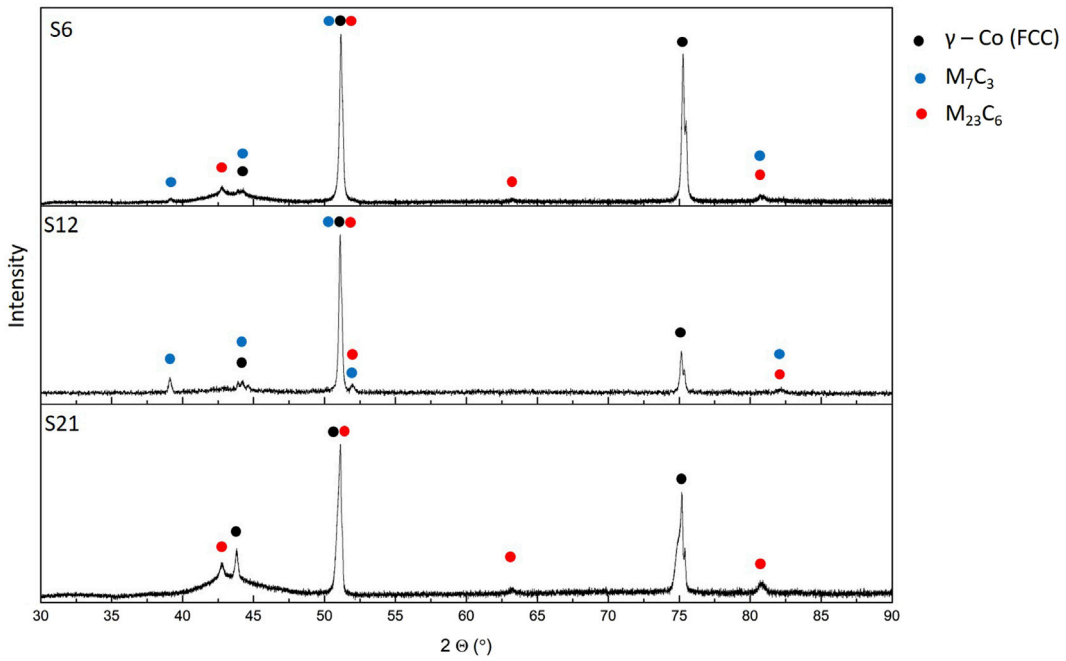

FIGURE 12
XRD patterns of the samples S6, S12, and S21.

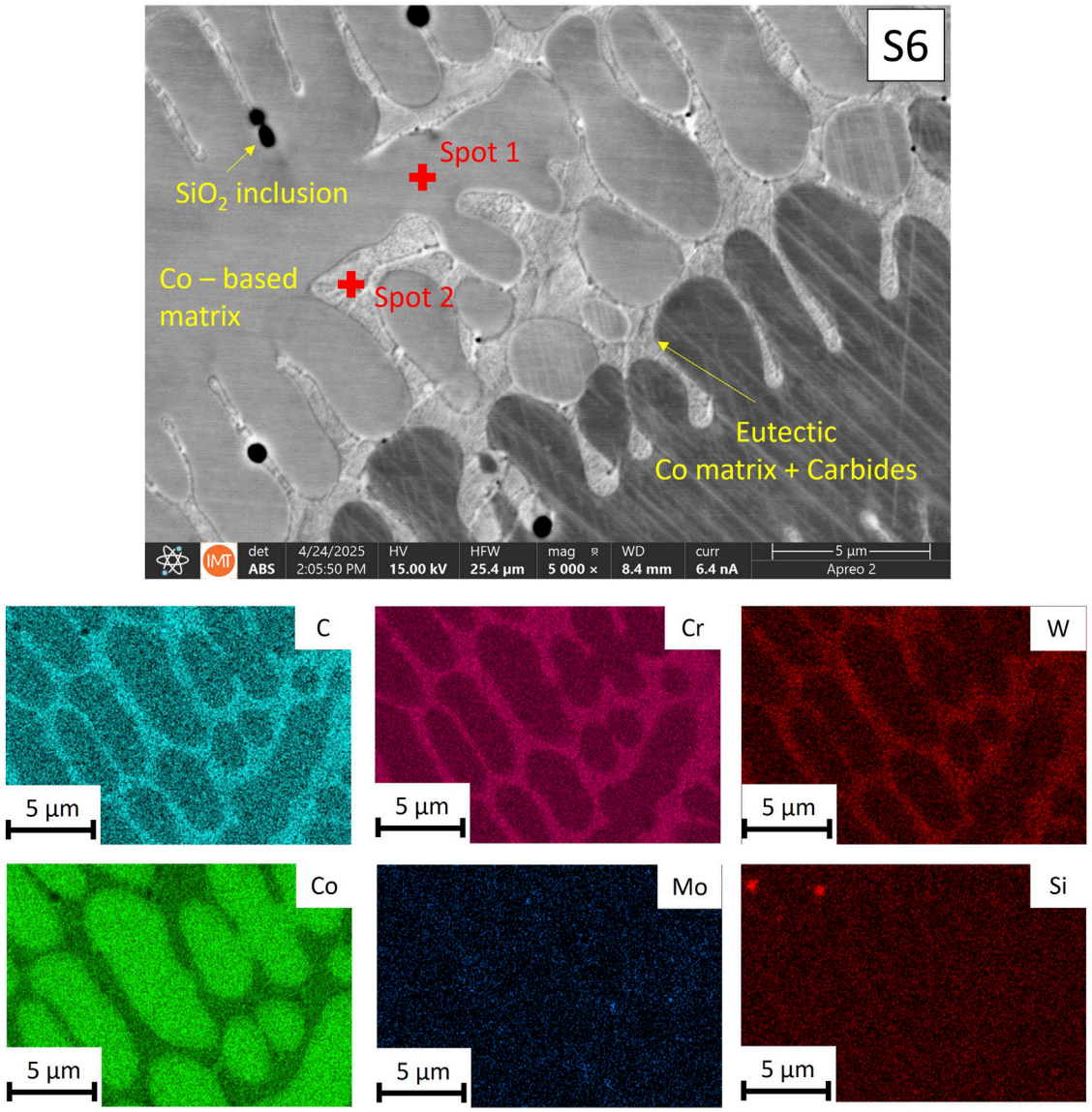

FIGURE 13
Backscattered SEM image of S6 samples and EDS elemental mapping of C, Cr, W, Co, Mo and Si.

3.5 SEM microstructure characterization

Figures 13–15 show SEM images of samples S6, S12, and S21, along with their corresponding EDS elemental mapping, EDS point analysis results are presented in Table 4. In sample S6, dendritic grains of the Co matrix exhibit an increased cobalt concentration. A fine eutectic structure, consisting of the Co matrix and carbides, is observed around the dendritic grains. The carbides are rich in Cr and W. Regions enriched with Mo are also detected between the dendritic grains, indicating the formation of Mo-rich carbides. Carbide types are confirmed using quantitative EDS point analyses (Table 4). M_7C_3 carbides show high Cr/Co ratios, $M_{23}C_6$ remain Cr-rich with lower Cr/Co ratios, whereas M_6C carbides exhibit strong W enrichment. Submicron-sized non-metallic inclusions of SiO_2 are present in the material. These inclusions are spherical in shape, suggesting that they formed in the melt and were pushed into the final solidification zone, where the eutectic developed. In sample S12, dendritic grains of the FCC Co matrix are present, with eutectic regions containing various carbides formed in the interdendritic areas. The eutectic grains in these regions are coarser in sample S12 due to slower solidification. Carbides rich in chromium (M_7C_3) are predominant, while W- and Co-rich carbides of the M_6C type are also observed. Sample S21 exhibits a homogeneous microstructure in which almost all alloying elements are dissolved in the Co matrix. Spherical non-metallic SiO_2 inclusions, formed in the melt, are also present in the microstructure. SiO_2 inclusions likely originate from the ferroalloy and minor oxidation in the melt. Their spherical morphology suggests formation in the liquid melt. Their size

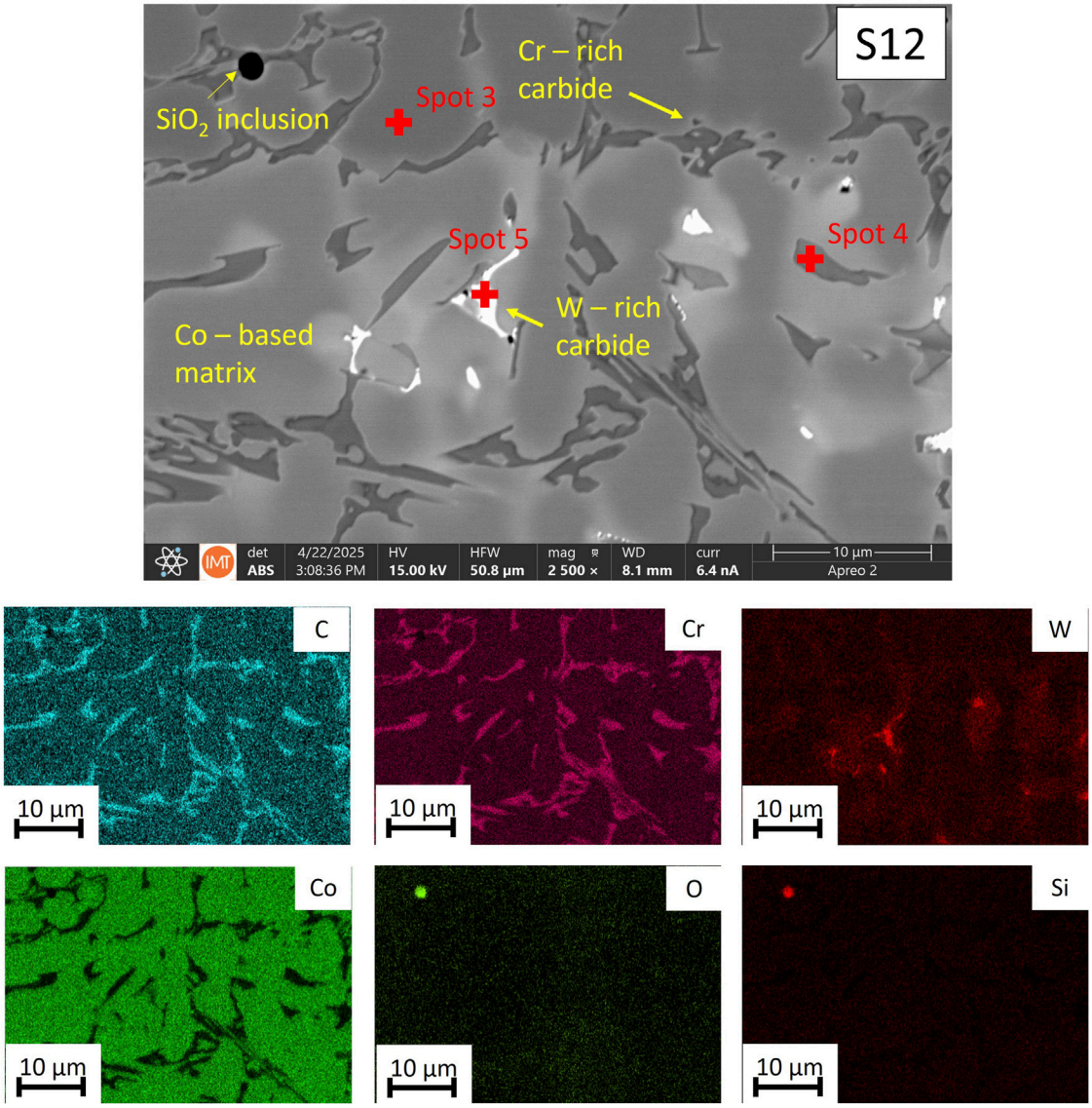

FIGURE 14
Backscattered SEM image of S12 samples and EDS elemental mapping of C, Cr, W, Co, O and Si.

(<1 µm) and distribution do not significantly affect hardness or eutectic uniformity.

Although equilibrium thermodynamic calculations predict the formation of the HCP phase, σ, µ, and M_6C carbides, these phases were not detected in any of the examined rods. This can be attributed to the non-equilibrium cooling conditions characteristic of horizontal continuous casting, where the actual cooling rates are significantly higher than those assumed under equilibrium conditions. The FCC to HCP transformation in Co-based alloys is known to be kinetically sluggish, requiring long-range diffusion and sufficiently slow cooling (Kuzucu et al., 1997; Davis, 2000; Kapoor et al., 2012; Narushima and Ueda, 2015; Chen et al., 2024; Li et al., 2025). Because the HCP phase is thermodynamically stable only within a narrow temperature window, the rapid extraction of heat suppresses atomic rearrangement and stabilizes the high-temperature FCC Co phase down to room temperature.While equilibrium thermodynamic calculations predict the formation of M_6C, σ, and µ phases, none of these were detected by XRD. This discrepancy is expected due to the extremely fast cooling in HCC, which suppresses solid-state diffusion required for their nucleation. The absence of σ and µ phases in XRD is therefore consistent with diffusion-limited transformation kinetics. This supports our conclusion that rapidly solidified HCC rods capture a metastable solidification microstructure.

Similarly, the precipitation of σ and µ intermetallic phases and late-stage M_6C carbides depend on extensive solid-state diffusion of Cr, Mo, and W, which is strongly limited at lower temperatures. The fine dendritic structure and short diffusion distances produced by rapid solidification prevent the chemical partitioning required for these phases to nucleate and grow (Bockus, 2006; Strzępek et al., 2025).

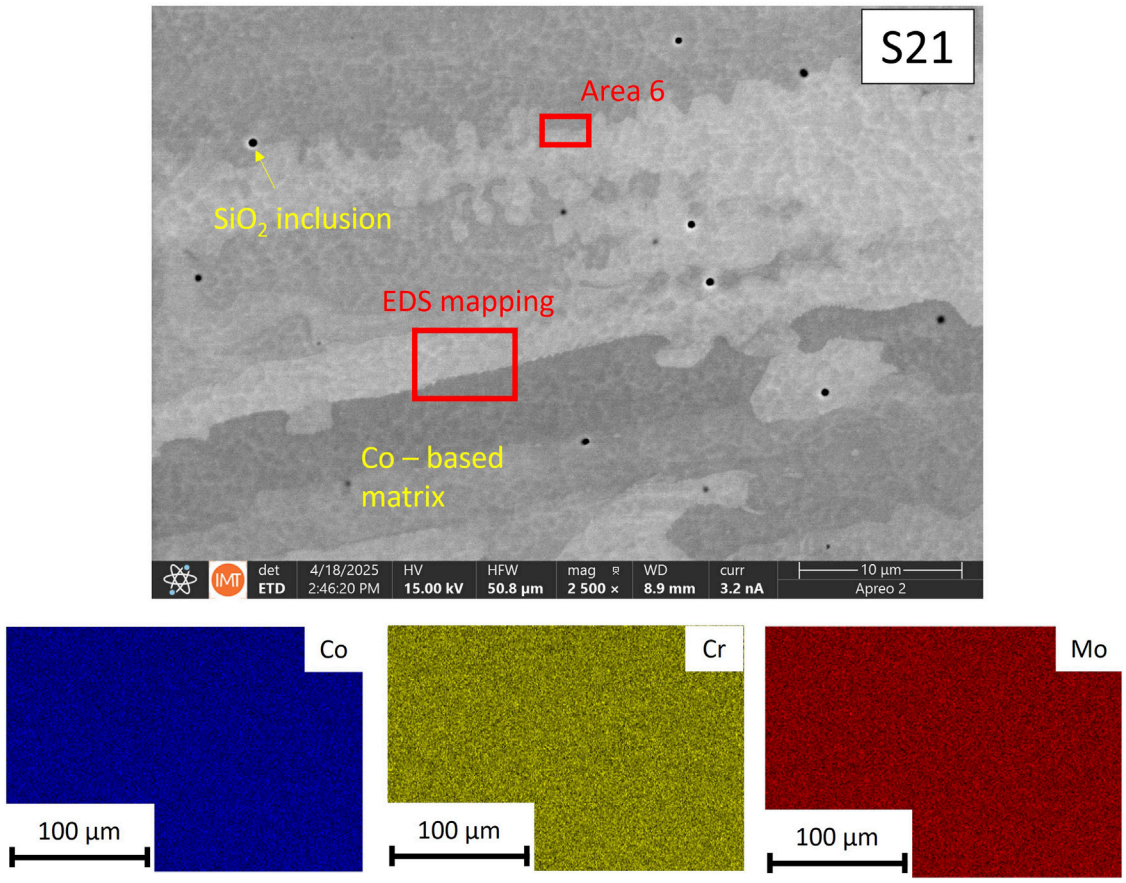

FIGURE 15
Backscattered SEM image of S21 samples and EDS elemental mapping of Co, Cr, and Mo.

TABLE 4 EDS microchemical composition of cast Stellite alloys, values in wt%.

Label	Si	Mn	Cr	Ni	Mo	W	Fe	Co
Spot 1	1.1	0.2	25.9	2.4	0.2	4.3	1.7	64.2
Spot 2	1.1	-	41.1	1.6	0.5	7.9	1.3	46.5
Spot 3	1.2	0.1	24.1	3.0	0.2	6.7	3.7	61.0
Spot 4	-	-	71.4	0.3	0.2	8.8	1.5	17.8
Spot 5	1.0	-	22.7	1.2	0.6	36.1	2.1	36.3
Spot 6	0.9	0.7	28.6	2.5	5.3	-	-	62.0

4 Conclusion

Based on the detailed microstructural characterisation of Stellite 6, 12, and 21 alloys produced by horizontal continuous casting (HCC), the following conclusions are established:

All alloys solidified into a primary FCC Co dendritic matrix with interdendritic carbides, and fine grains across the rod cross-sections, due to high cooling rates of 200–500 K/s.

There are no solid-state transformations as confirmed by the X-ray Diffraction (XRD) analysis. More specifically, the suppression of solid-state phase transformations of both the matrix FCC to HCP and carbide M_7C_3 to $M_{23}C_6$, nor intermetallic phase formation despite thermodynamic predictions.

The results show that fine grains and homogeneous carbide distribution are key to high hardness, as alloys with slightly lower carbon achieved higher hardness values, due to finer microstructure. However, when the carbide content is too low, hardness decreases significantly. Solid solution strengthening of the Co matrix is of secondary meaning when aiming at high hardness values. The refining of the eutectic carbide network with high solidification and cooling rates is an effective way to increase hardness.

The fine and homogeneous microstructures make the HCC rods well suited for hard-facing feedstock, where chemical uniformity is especially beneficial for forming wear-resistant layers.

The present study does not include wear testing or high-temperature evaluations, which are essential for linking microstructure to functional performance. Future work should also evaluate scale-up effects for larger diameters.

Data availability statement

The raw data supporting the conclusions of this article will be made available by the authors, without undue reservation.

Author contributions

AB: Data curation, Formal Analysis, Visualization, Methodology, Conceptualization, Writing – original draft, Investigation, Resources. JB: Conceptualization, Investigation, Resources, Supervision, Writing – review and editing, Methodology.

Funding

The author(s) declared that financial support was received for this work and/or its publication. This research was funded by ARIS research program P2-0050.

Conflict of interest

Author AB was employed by Metal Tech Solutions.

The remaining author(s) declared that this work was conducted in the absence of any commercial or financial relationships that could be construed as a potential conflict of interest.

Generative AI statement

The author(s) declared that generative AI was not used in the creation of this manuscript.

Any alternative text (alt text) provided alongside figures in this article has been generated by Frontiers with the support of artificial intelligence and reasonable efforts have been made to ensure accuracy, including review by the authors wherever possible. If you identify any issues, please contact us.

Publisher's note

References

Ahmed, R., de Villiers Lovelock, H. L., and Davies, S. (2021). Sliding wear of blended cobalt based alloys. *Wear* 466-467, 466–467. doi:10.1016/j.wear.2020.203533

Ahmed, M. (2024). "Demonstration of a high-performance continuous casting process for cobalt alloy ASTM F75," in *MATEC web of conferences* (Glasgow, Scotland, United Kingdom: EDP Sciences) 09001. doi:10.1051/matecconf/202440109001

Ahmed, R., Fardan, A., and Davies, S. (2024). Mapping the mechanical properties of cobalt-based stellite alloys manufactured *via* blending. *Adv. Mater. Process. Technol.* 10 (3), 2531–2560. doi:10.1080/2374068X.2023.2220242

Aoh, J. N., and Chen, J. C. (2001). On the wear characteristics of cobalt-based hardfacing layer after thermal fatigue and oxidation. *Wear* 250 (PART 1), 611–620. doi:10.1016/S0043-1648(01)00668-8

Bockus, S. (2006). A study of the microstructure and mechanical properties of continuously cast iron products. *Metalurgija* 45 (4), 287290.

Chen, W., Liu, B., Chen, L., Xu, J., and Zhu, Y. (2020). Effect of laser cladding stellite 6-cr3c2-ws2 self-lubricating composite coating on wear resistance and microstructure of H13. *Metals* 10 (6), 1–12. doi:10.3390/met10060785

Chen, B., Chen, R., Fan, Y., Chen, Z., and Zhao, Z. (2024). Microstructural characterization of stellite 6 alloy processed by electron beam melting. *Vacuum* 229 (July), 113591. doi:10.1016/j.vacuum.2024.113591

Codaro, E. N., Melnikov, P., Ramires, I., and Guastaldi, A. C. (2000). Corrosion behavior of a cobalt-chromium-molybdenum alloy. *Russ. J. Electrochem.* 36 (10), 1263–1267. doi:10.1007/bf02757531

Davis, J. R. (2000). *ASM specialty handbook: nickel, cobalt, and their alloys*. Materials Park, Ohio: ASM International.

Frenk, A., and Kurz, W. (1994). Microstructural effects on the sliding wear resistance of a cobalt-based alloy. *Wear* 174 (1–2), 81–91. doi:10.1016/0043-1648(94)90089-2

Hou, Q. Y., Gao, J. S., and Zhou, F. (2005). Microstructure and wear characteristics of cobalt-based alloy deposited by plasma transferred arc weld surfacing. *Surf. Coatings Technol.* 194 (2–3), 238–243. doi:10.1016/j.surfcoat.2004.07.065

Hu, P., Liu, R., Liu, J., McRae, G., Yao, M. X., and Collier, R. (2014). Advanced stellite alloys with improved metal-on-metal bearing for hip implants. *Mater. Des.* 60, 424–432. doi:10.1016/j.matdes.2014.04.007

Huang, P., Liu, R., Wu, X., and Yao, M. X. (2007). Effects of molybdenum content and heat treatment on mechanical and tribological properties of a low-carbon stellite® alloy. *J. Eng. Mater. Technol.* 129 (4), 523–529. doi:10.1115/1.2744429

Kapoor, S. (2012). Temperature-dependence of hardness and wear resistance of stellite alloys. *Int. J. Mater. Metallurgical Eng.* 6 (7), 592–601. doi:10.5281/ZENODO.1060871

Karaali, A., Mirouh, K., Hamamda, S., and Guiraldenq, P. (2005). Microstructural study of tungsten influence on Co-Cr alloys. *Mater. Sci. Eng. A* 390 (1–2), 255–259. doi:10.1016/j.msea.2004.08.001

Karthik, S. R., Londe, N. V., Shetty, R., Nayak, R., and Hedge, A. (2022). Optimization and prediction of hardness, wear and surface roughness on age hardened stellite 6 alloys. *Manuf. Rev.* 9, 10. doi:10.1051/mfreview/2022008

Khan, M. F., Damodaram, R., Altammar, H., and Karthik, G. M. (2025). Metallurgical and mechanical properties of stellite 6 deposition developed through friction surfacing technique. *Materials* 18 (5), 1003. doi:10.3390/ma18051003

Kofstad, P. K., and Hed, A. Z. (1969a). High temperature oxidation of Co-10 w/o Cr alloys. II - oxidation kinetics. *J. Electrochem. Soc.* 116 (2), 229–234. doi:10.1149/1.2411803

Kofstad, P. K., and Hed, A. Z. (1969b). Oxidation of Co-25 w/o Cr at high temperatures. *J. Electrochem. Soc.* 116 (11), 1542. doi:10.1149/1.2411603

Krell, J., Röttger, A., and Theisen, W. (2020). Comprehensive investigation of the microstructure-property relationship of differently manufactured co–cr–c alloys at room and elevated temperature. *Wear*, 444–445. doi:10.1016/j.wear.2019.203138

Kurosu, S., Matsumoto, H., and Chiba, A. (2010). Isothermal phase transformation in biomedical Co-29Cr-6Mo alloy without addition of carbon or nitrogen. *Metallurgical Mater. Trans. A Phys. Metallurgy Mater. Sci.* 41 (10), 2613–2625. doi:10.1007/s11661-010-0273-8

Kuzucu, V., Ceylan, M., Çelik, H., and Aksoy, İ. (1997). Microstructure and phase analyses of stellite 6 plus 6 wt.% Mo alloy. *J. Mater. Process. Technol.* 69 (1–3), 257–263. doi:10.1016/S0924-0136(97)00027-7

Li, Y., Tang, N., Tunthawiroon, P., Koizumi, Y., and Chiba, A. (2013). Characterisation of oxide films formed on Co-29Cr-6Mo alloy used in die-casting moulds for aluminium. *Corros. Sci.* 73, 72–79. doi:10.1016/j.corsci.2013.03.026

Li, S. Q., Wu, X. Y., Liu, R., Yao, M. X., and Wang, Z. Q. (2025). Microstructural characteristics of stellite 21 alloy manufactured with different processes. *Metallogr. Microstruct. Analysis* 14, 176–188. doi:10.1007/s13632-025-01166-6

Liu, R., Yao, J., Zhang, Q., Yao, M. X., and Collier, R. (2015). Effects of molybdenum content on the wear/erosion and corrosion performance of low-carbon stellite alloys. *Mater. Des.* 78, 95–106. doi:10.1016/j.matdes.2015.04.030

Liu, R., Yao, J. H., Zhang, Q. L., Yao, M. X., and Collier, R. (2015). Relations of chemical composition to solidification behavior and associated microstructure of stellite alloys. *Metallogr. Microstruct. Analysis* 4 (3), 146–157. doi:10.1007/s13632-015-0196-2

Lu, Y., Wu, S., Gan, Y., Zhang, S., Guo, S., Lin, J., et al. (2016). Microstructure, mechanical property and metal release of As-SLM CoCrW alloy under different solution treatment conditions. *J. Mech. Behav. Biomed. Mater.* 55, 179–190. doi:10.1016/j.jmbbm.2015.10.019

Motallebzadeh, A., Atar, E., and Cimenoglu, H. (2015). Sliding wear characteristics of molybdenum containing stellite 12 coating at elevated temperatures. *Tribol. Int.* 91, 40–47. doi:10.1016/j.triboint.2015.06.006

Narushima, T., Ueda, K., and Alfirano, (2015). "Co-Cr alloys as effective metallic biomaterials," in *Advances in metallic biomaterials* (Berlin, Heidelberg: Springer), 157–178. doi:10.1007/978-3-662-46836-4_7

Nová, K., Novák, P., and Dvorský, D. (2017). Influence of alloying elements on the mechanical properties of a cobalt-based alloy produced with powder metallurgy. *Materiali Tehnologije* 51 (3), 443–447. doi:10.17222/mit.2016.054

Pala, Z., Bai, M., Lukac, F., and Hussain, T. (2017). Laser clad and HVOF-sprayed stellite 6 coating in chlorine-rich environment with KCl at 700 °C. *Oxid. Metals* 88 (5–6), 749–771. doi:10.1007/s11085-017-9776-7

Petrík, J., and Palfy, P. (2011). The influence of the load on the hardness. *Metrology Meas. Syst.* 18 (2), 5. doi:10.2478/v10178-011-0005-5

Phalnikar, C. A., Evans, E. B., and Baldwin, W. M. (1956). High temperature scaling of cobalt-chromium alloys. *J. Electrochem. Soc.* 103 (8), 429. doi:10.1149/1.2430374

Radu, I., and Li, D. Y. (2005). Investigation of the role of oxide scale on stellite 21 modified with yttrium in resisting wear at elevated temperatures. *Wear* 259 (1–6), 453–458. doi:10.1016/j.wear.2005.01.022

Radu, I., Li, D. Y., and Llewellyn, R. (2004). Tribological behavior of stellite 21 modified with yttrium. *Wear* 257 (11), 1154–1166. doi:10.1016/j.wear.2004.07.013

Ravi Kumar, L. (2020). "An experimental investigation on wear characteristics of C-45 grade steel overlay with stellite," in *IOP conference series: materials science and engineering* (Chennai, India: IOP Publishing Ltd). doi:10.1088/1757-899X/988/1/012039

Roy, S., Sridharan, N., Cakmak, E., Ghaednia, H., Gangopadhyay, A., and Qu, J. (2021). Post weld heat treatment and operating temperature effect on tribological behavior of laser cladded stellite 21 coating. *Wear* 482–483 (May), 203990. doi:10.1016/j.wear.2021.203990

Saldívar-García, A. J., and López, H. F. (2005). Microstructural effects on the wear resistance of wrought and as-cast Co-Cr-Mo-C implant alloys. *J. Biomed. Mater. Res. - Part A* 74 (2), 269–274. doi:10.1002/jbm.a.30392

Shin, J. C., Doh, J. M., Yoon, J. K., Lee, D. Y., and Kim, J. S. (2003). Effect of molybdenum on the microstructure and wear resistance of cobalt-base stellite hardfacing alloys. *Surf. Coatings Technol.* 166 (2–3), 117–126. doi:10.1016/S0257-8972(02)00853-8

Smolina, I., and Kobiela, K. (2021). Characterization of wear and corrosion resistance of stellite 6 laser surfaced alloyed (lsa) with rhenium. *Coatings* 11 (3), 1–16. doi:10.3390/coatings11030292

Strzępek, P., Mamala, A., Boumerzoug, Z., Baudin, T., Brisset, F., Zasadzińska, M., et al. (2025). Effect of horizontal continuous casting parameters on cyclic macrosegregation, microstructure, and properties of high-strength Cu–Mg alloy cast rod. *Metallurgical Mater. Trans. A Phys. Metallurgy Mater. Sci.* 56 (1), 41–60. doi:10.1007/s11661-024-07609-z

Tunthawiroon, P., and Chiba, A. (2019). Characterization of intermetallic phase in as-cast Si-doped co-cr-mo alloys. *IOP Conf. Ser. Mater. Sci. Eng.* 635 (1), 012007. doi:10.1088/1757-899X/635/1/012007

Tunthawiroon, P. (2020). Xps analysis of oxide formed on the surface of Co-28Cr-6Mo-1Si alloy oxidized at 550 °C. *Key Eng. Mater.* 845 KEM, 95–100. doi:10.4028/www.scientific.net/KEM.845.95

Wang, S. Y., Hou, X. Y., Wang, L., Zhang, H. Y., Zhang, W. B., Xia, Y. P., et al. (2021). Effect of ball-milling process in combination with the addition of carbide microparticles on the microstructure and wear resistance of a Co-Cr-W alloy prepared by powder metallurgy method. *Mater. Res. Express* 8 (6), 066506. doi:10.1088/2053-1591/ac021f

Xiong, J., Guo, Y., Nie, F., Mao, G., Yang, J., Zhou, Q., et al. (2023). Temporal evolution of microstructure and its influence on micromechanical and tribological properties of Stellite-6 cladding under aging treatment. *J. Mater. Sci.* 58 (26), 10802–10820. doi:10.1007/s10853-023-08690-2

Yao, Z., Chen, Z., Ouyang, M., Chen, X., Yang, M., Li, Z., et al. (2023). Accelerated discovery of composition-carbide-hardness linkage of stellite alloys assisted by image recognition. *Scr. Mater.* 234, 115539. doi:10.1016/j.scriptamat.2023.115539

Zhao, Y., Ge, C., Wu, Y., Deng, Y., Zhang, W., Liu, X., et al. (2024). The impact of Nb on the microstructure and mechanical properties of stellite 21 alloy coatings. *Surf. Coatings Technol.* 489, 131113. doi:10.1016/j.surfcoat.2024.131113